The Astrophysical Journal, 814:68 (12pp), 2015 November 20 doi:10.1088/0004-637X/814/1/68
© 2015. The American Astronomical Society. All rights reserved.

3D ELECTRON DENSITY DISTRIBUTIONS IN THE SOLAR CORONA DURING SOLAR MINIMA: ASSESSMENT FOR MORE REALISTIC SOLAR WIND MODELING

Judith de Patoul[1,2], Claire Foullon[1], and Pete Riley[3]
[1] University of Exeter, Exeter, Devon EX4, UK; j.depatoul@exeter.ac.uk, c.foullon@exeter.ac.uk
[2] Laboratoire d'Astrophysique de Marseille, UMR 7326, CNRS and Aix-Marseille Université, 38 Rue Frédéric Joliot-Curie, F-13388 Marseille cedex 13, France
[3] Predictive Science, 9990 Mesa Rim Road, Suite 170, San Diego, CA 92121, USA; rileype@saic.com
Received 2015 July 31; accepted 2015 October 15; published 2015 November 17

ABSTRACT

Knowledge of the electron density distribution in the solar corona put constraints on the magnetic field configurations for coronal modeling and on initial conditions for solar wind modeling. We work with polarized *SOHO*/LASCO-C2 images from the last two recent minima of solar activity (1996–1997 and 2008–2010), devoid of coronal mass ejections. The goals are to derive the 4D electron density distributions in the corona by applying a newly developed time-dependent tomographic reconstruction method and to compare the results between the two solar minima and with two magnetohydrodynamic models. First, we confirm that the values of the density distribution in thermodynamic models are more realistic than in polytropic ones. The tomography provides more accurate distributions in the polar regions, and we find that the density in tomographic and thermodynamic solutions varies with the solar cycle in both polar and equatorial regions. Second, we find that the highest-density structures do not always correspond to the predicted large-scale heliospheric current sheet or its helmet streamer but can follow the locations of pseudo-streamers. We deduce that tomography offers reliable density distributions in the corona, reproducing the slow time evolution of coronal structures, without prior knowledge of the coronal magnetic field over a full rotation. Finally, we suggest that the highest-density structures show a differential rotation well above the surface depending on how they are magnetically connected to the surface. Such valuable information on the rotation of large-scale structures could help to connect the sources of the solar wind to their in situ counterparts in future missions such as *Solar Orbiter* and *Solar Probe Plus*.

Key words: solar wind – Sun: corona – Sun: evolution – Sun: fundamental parameters – Sun: rotation

1. INTRODUCTION

The distribution of the magnetic field generated in the solar interior and connected into the solar wind influences most coronal phenomena, including large-scale and slowly evolving coronal structures. The coronal density distribution can serve as a tracer of the configuration of the magnetic field (shape and general morphology rather than field strength), since the coronal plasma is frozen into the field (for a review see, e.g., Wiegelmann et al. 2014). Of particular interest are the observations of streamers and pseudo-streamers, referring to structures associated with large magnetic loops that separate coronal holes of opposite polarity and twin loop arcades that separate coronal holes of the same polarity, respectively (Wang et al. 2007). Another example is the study of magnetic structures above the solar polar regions, where the measurements of the line-of-sight (LOS) magnetograms are generally less reliable owing to the larger viewing angle with the magnetic field. The observed electron density distributions in coronal holes and polar plumes (Barbey et al. 2008; de Patoul et al. 2013b) could provide a better understanding of how the flux emergence near the equator affects the magnetic field configuration at the pole (de Patoul et al. 2013a). Finally, an accurate determination of the ambient coronal electron density provides a better estimation of the mass and the propagation of coronal mass ejections (CMEs; Vourlidas et al. 2000; Feng et al. 2015a, 2015b). In particular, the density is important for calculating the compression ratio of CME-driven shocks and the Alfvén Mach number, which has important implications for the localization of particle acceleration sites and hence space weather forecasts (Bemporad & Mancuso 2011; Chen et al. 2014).

The first proposed empirical approach to obtain the electron density from remote sensing observations was an inversion method using measurements from eclipses in polarized white light, with the assumption that the coronal electron density is axisymmetric (van de Hulst 1950). Saito et al. (1977) used this method to calculate electron densities from polarized brightness (pB) observations obtained by *Skylab* coronagraph data during the declining phase of the solar cycle from 1973 May to 1974 February. A good agreement of the density values was found using *SOHO*/LASCO-C2 data during 1998 February (Hayes et al. 2001) and 1996 December (Quémerais & Lamy 2002). Empirical methods to obtain the full 3D density distribution are given by solar rotational tomography (SRT). SRT has been specifically developed for optically thin structures and uses LOS-integrated coronal images from multiple viewpoints taking advantage of solar rotation. White-light images of the K-corona, where the radiation is dominated by Thomson scattering, can be used to reconstruct density from 1.5 $R_\odot$ up to 6.5 $R_\odot$ using images from the LASCO-C2 or *STEREO*/COR1 (e.g., Frazin 2000; Barbey et al. 2013; Kramar et al. 2014; Peillon et al. 2015). When the sources for a tomographic inversion are EUV images, both density and temperature can be reconstructed by applying differential emission measure tomography (Frazin et al. 2009). However, even in the best cases, only reconstruction close to the surface from about 1.03 $R_\odot$ to 1.25 $R_\odot$ can be obtained. An alternative physics-based approach to obtain a quantitative 3D density distribution is given by magnetohydrodynamic (MHD) models, which provide the global configuration of the magnetic field and the plasma parameters (i.e., density, temperature, and velocity) in the corona (Riley et al. 2001, 2006; Lionello et al. 2009).

Here we determine the electron density distribution in the corona during the two previous solar minima: 1996–1997 (solar cycle number 22/23) and 2008–2010 (solar cycle number 23/24). In Section 2, we determine the 4D electron density distribution (N_e) from a newly developed time-dependent tomographic method. We look at the general morphology of the density structures in the empirical model from tomography and compare with a simple potential field source surface (PFSS) model and more advanced MHD models. In Section 3, we contrast the density values found by tomography and the ones predicted by MHD models; especially, we discuss (1) the temporal and radial profiles of the density, (2) the location of the helmet streamer and pseudo-streamer, and (3) the presence of a differential rotation of the structures in the corona.

2. DETERMINATION OF THE ELECTRON DENSITY DISTRIBUTION

2.1. N_e from Tomography

Since 1996 the *SOHO*/LASCO-C2 coronagraph has continuously produced sets of white-light and polarized images of the solar corona with a field of view ranging from about 1.5 $R_\odot$ up to 6.5 $R_\odot$ (Brueckner et al. 1995). To determine the electron density distribution (N_e) in the corona, we use the pB images that are extracted from the total brightness LASCO-C2 images pre-processed as described by Llebaria et al. (2006), Gardès et al. (2013), and Lamy et al. (2014). The resulting pB images are dominated by the electron-scattered K corona, which is known to be strongly polarized (Billings 1966), and not contaminated by the dust-scattered F corona, which is essentially unpolarized at low heights and has been removed during the calibration. The intensity measured in pB images, $I_{\rm pB}$, observed from a view direction at a rotation angle, ϑ, of the Sun relative to the observer's longitude, is the integration of the electron density, N_e, along the LOS direction, $\boldsymbol{e}_{\rm LOS}(\vartheta)$,

$$I_{\rm pB}(\rho, \vartheta) = \int_{\rm LOS} N_e\Big(\boldsymbol{r}\big(l\ \boldsymbol{e}_{\rm LOS}(\vartheta)\big)\Big) \times K\Big(\boldsymbol{r}\big(l\ \boldsymbol{e}_{\rm LOS}(\vartheta)\big),\ \rho\ \boldsymbol{e}^{\perp}_{\rm LOS}(\vartheta)\Big)\, dl, \quad (1)$$

where $\boldsymbol{e}^{\perp}_{\rm LOS}$ is the vector unit orthogonal to $\boldsymbol{e}_{\rm LOS}$, ρ is the distance from the Sun center to $\boldsymbol{e}_{\rm LOS}$, and $\boldsymbol{r}$ is the radial vector. The Thomson scattering function, K, is defined for a point source of luminosity, $4\pi L$, by (Frazin et al. 2010)

$$K = \frac{3\sigma_e}{16}\frac{L}{\rho^2}\sin^4\Theta, \quad (2)$$

where Θ is the scattering angle defined by $\sin\Theta = \dfrac{\rho}{\|\boldsymbol{r}(l\ \boldsymbol{e}_{\rm LOS}(\vartheta))\|}$ and σ_e is the Thomson scattering cross section for a single electron. A typical example of a pB image is shown in Figure 1 (top panel), where a background subtraction has been applied to enhance the intensity along the radial direction. In this work, we consider coronal heights above 2.5 $R_\odot$ to avoid artifacts due to diffraction surrounding the occulter. The pB image shown in Figure 1 (top panel) was taken when a CME occurred at a position angle of 271°. This CME had an angular width of 114.1° and traversed the corona from 2.5 to 7.5 $R_\odot$ in approximately 2.5 hr (Boursier et al. 2009). Solar rotational tomographic methods cannot resolve fast temporal changes, and important artifacts are produced in the reconstructions. To minimize this effect, we remove the CMEs from the pB images. Morgan & Habbal (2010) proposed a method for separating CMEs from the quiescent corona in white-light coronagraph images based on the fact that the large-scale structures are close to radial, while CMEs are highly nonradial. Here we consider CMEs listed in the CACTus (Robbrecht & Berghmans 2004) and the ARTEMIS (Boursier et al. 2009) catalogs that have an intensity larger than 0.8×10^3 W sr^{-1} m^{-2}. Using the position angle and angular width from these catalogs, we simply exclude the angular portion of the pB image affected by the CME from the tomographic reconstruction procedure (Figure 1, bottom panel).

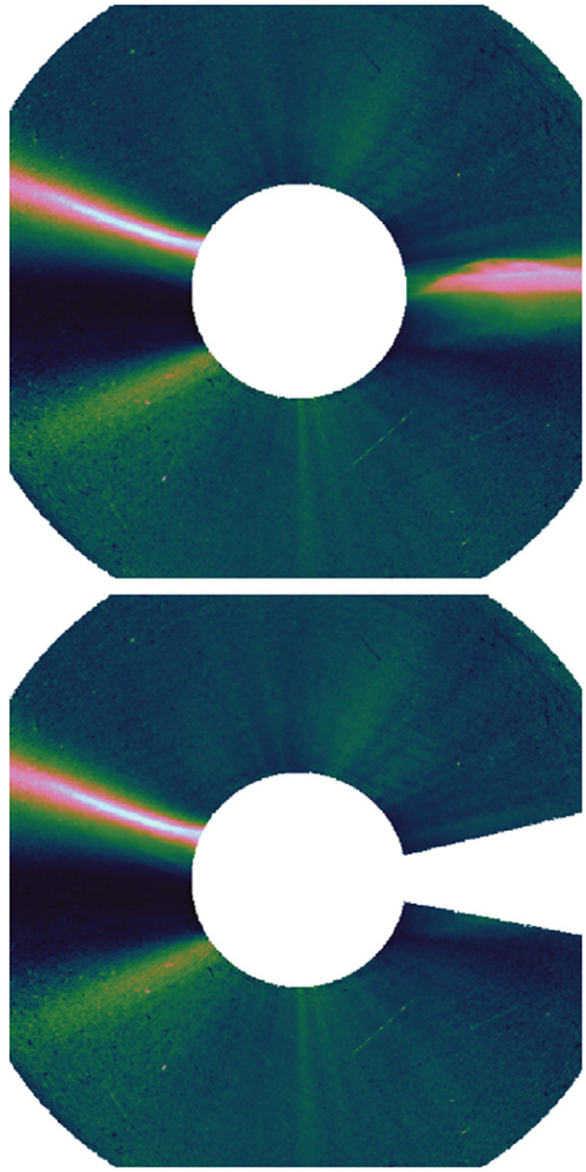

Figure 1. *SOHO*/LASCO-C2 pB image taken on 2008 March 26 at 20:56UT. The field of view is shown from 2.5 to 6.5 $R_\odot$. A contrast enhancement has been applied to increase the intensity in the radial direction. Top: pB image with a CME observed. Bottom: same image with the angular portion of the CME, which is excluded from the tomographic procedure.

The electron density is obtained by inverting Equation (1) using SRT. We use the newly developed time-dependent tomographic method, which has been elaborated and described by Peillon et al. (2014, 2015). The method involves spatio-temporal regularization (Kalman filters) to mitigate the slow temporal variation of the corona and assumes a nearly solid rotation of the Sun of 27.2753 days, corresponding to the Carrington rotation. It requires a continuous set of view directions uniformly distributed over half a rotation, with a minimum cadence of one pB image per day, i.e., a number of $n_I \geqslant 13$ images for a given tomography reconstruction. The corona is divided into a spherical grid $(r, \phi, \theta; t)$ with a size of $(60 \times 60 \times 120 \times n_I)$, covering the heliocentric distances from 2.5 to 8.5 $R_\odot$. To assess the robustness and accuracy of the technique, the method has been tested using a set of 14 projected images of a time-dependent MHD volume as "observations." The result could successfully reproduce the slow time-varying dynamic of the model. The estimated density distribution, $\tilde{\boldsymbol{x}}$, is constructed on the grid cells by solving the following least-squares minimization problem:

$$\tilde{\boldsymbol{x}} = \underset{\boldsymbol{x} \geqslant 0}{\operatorname{argmin}} \left\{ \|\boldsymbol{y} - \boldsymbol{A}\boldsymbol{x}\|_2^2 + \lambda_S^2 \|\boldsymbol{R}_S \boldsymbol{x}\|_2^2 + \lambda_T^2 \|\boldsymbol{R}_T \boldsymbol{x}\|_2^2 + \lambda_C^2 \|\boldsymbol{R}_C \boldsymbol{x}\|_2^2 \right\}. \quad (3)$$

The vector $\boldsymbol{y}$ contains the intensity measured in each pixel from the set of pB images over half a rotation, i.e., the $I_{\mathrm{pB}}(\rho_{ij}, \vartheta)$ defined in Equation (1) with $\vartheta \in [0, 2\pi]$ and ρ_{ij} giving the position of the pixel in the image. The vector $\boldsymbol{x}$ contains N_{e} values defined in the spherical grid $(r, \phi, \theta; t)$. $\boldsymbol{A}$ is a diagonal-like matrix composed of blocks of projection matrices that are determined by the geometry and the physics of the problem, i.e., the relation between the volume element in $\boldsymbol{x}$ and the LOS-related pixel in the pB image defined by Thomson scattering function (2). The matrices $\boldsymbol{R}_S$, $\boldsymbol{R}_T$, and $\boldsymbol{R}_C$ in Equation (3) are the spatio-temporal regularization terms, which introduce a prior knowledge of the solution. This regularization minimizes the effects of the noise, the limited number of pB images available, and the unavoidable temporal change in the corona. The spatial regularization matrix, $\boldsymbol{R}_S$, described in Frazin et al. (2007), is a second derivative of the angular spherical coordinates θ and ϕ, multiplied by r^{-1} to reduce the radial distance noise. The temporal regularization matrix, $\boldsymbol{R}_T$, is a first derivative to enforce smoothness between two successive views of the Sun. The co-rotating regularization matrix, $\boldsymbol{R}_C$, is acting jointly in the spacetime domain. Its purpose is to prevent the reconstruction from concentrating material in the vicinity of the plane of the sky (containing the Sun's center). This is a plane that rotates in the Carrington coordinate system, and it is always orthogonal to the observer's LOS. The regularization parameters, $(\lambda_S, \lambda_T, \lambda_C)$, are estimated by minimizing the normalized rms error of the time-dependent 3D MHD model and its reconstruction ($\lambda_S = 2.2 \times 10^{-6}$, $\lambda_T = 1.7 \times 10^{-6}$, and $\lambda_C = 0.2 \times 10^{-6}$). Further details about the method and the construction of these regularization operators can be found in Peillon et al. (2015); see, in particular, discussion on the use of the temporal regularization, including examples of 3D and 4D tomographic reconstruction.

A full 4D reconstruction is performed every 4 days, provided that a minimum of 13 pB images are available. During 1996–1997, several data gaps are present for which the tomography was not carried out. Panel (a) of Figure 2 shows a typical result from tomography during a relatively quiet period of the solar activity when the number of CMEs is reduced. It was obtained using 14 pB images from 2008 November 21 to December 4, which is included in Carrington rotation 2077. The left panel of Figure 2(a) shows the 2D longitude–latitude map at 3.5 $R_\odot$ centered on 2008 December 2. The right panel shows the latitude–radial average map constructed by integrating over the longitudes (a radial contrast enhancement has been applied). It helps to represent the extent to which the helmet streamer spreads over the latitudes during this particular period. Panel (a) of Figure 3 shows another result from tomography in the later phase of the extended solar minimum, when solar activity has started to increase. It was obtained using 15 pB images from 2010 June 6 to 20, during Carrington rotation 2097. The latitudinal positions of the maximum of density evaluated for each longitude in the tomographic reconstruction are indicated by the white dots. Some voxels near the higher-density structure have a density value close to zero, for example, Figure 2(a), the region at longitude [30°, 34°] and latitude [−29°, −32°]. These zero-density artifacts are usually caused by the unavoidable rapid change in the corona. Indeed, the inverse problem can set a negative value to account for an unexplained variation of intensity in the data from a single viewpoint (Barbey et al. 2013). This could also be caused by remaining instrumental artifacts in a pB image.

2.2. N_e from MHD Models

The PFSS model is a simple and popular current-free model capable of reproducing the basic coronal magnetic field configuration. It requires only the synoptic maps of the LOS photospheric magnetic field component as a lower boundary, and it assumes that all field lines become radial at the upper boundary (the source surface) at about 2.5–3.5 $R_\odot$. The global magnetic field configuration predicted by the PFSS model can be used as a proxy of the density distribution in the corona. In particular, the neutral line at the source surface, which separates the large-scale opposite-polarity regimes of the coronal magnetic field, is often used to locate the heliospheric current sheet (HCS) and the helmet streamer. The PFSS/HCS calculated for a source surface at 2.5 $R_\odot$ is displayed as the black line in Figures 2 and 3.

A more complex and elaborate way to predict the magnetic field configuration and the density distribution in the corona is to employ global MHD models. We use solutions from MHD models developed by the group at Predictive Science (Riley et al. 2001, 2006; Lionello et al. 2009; see online, www.predsci.com). For the lower boundary condition, the models use the radial component of the magnetic field provided by the observed LOS measurements of *SOHO*/MDI magnetograms and uniform characteristic values for the plasma density and temperature. It assumes also that the electron and proton density are equal. In the polytropic MHD model, the energy equation is approximated by a simple adiabatic energy equation with a polytropic index $\gamma = 1.05$. Since this approximation significantly simplifies the problem and reduces the time necessary to complete a simulation, its solutions can be obtained more routinely and are available between 1 and 30 $R_\odot$ for all the Carrington rotations under study. This model reproduces well the geometrical and topological properties of

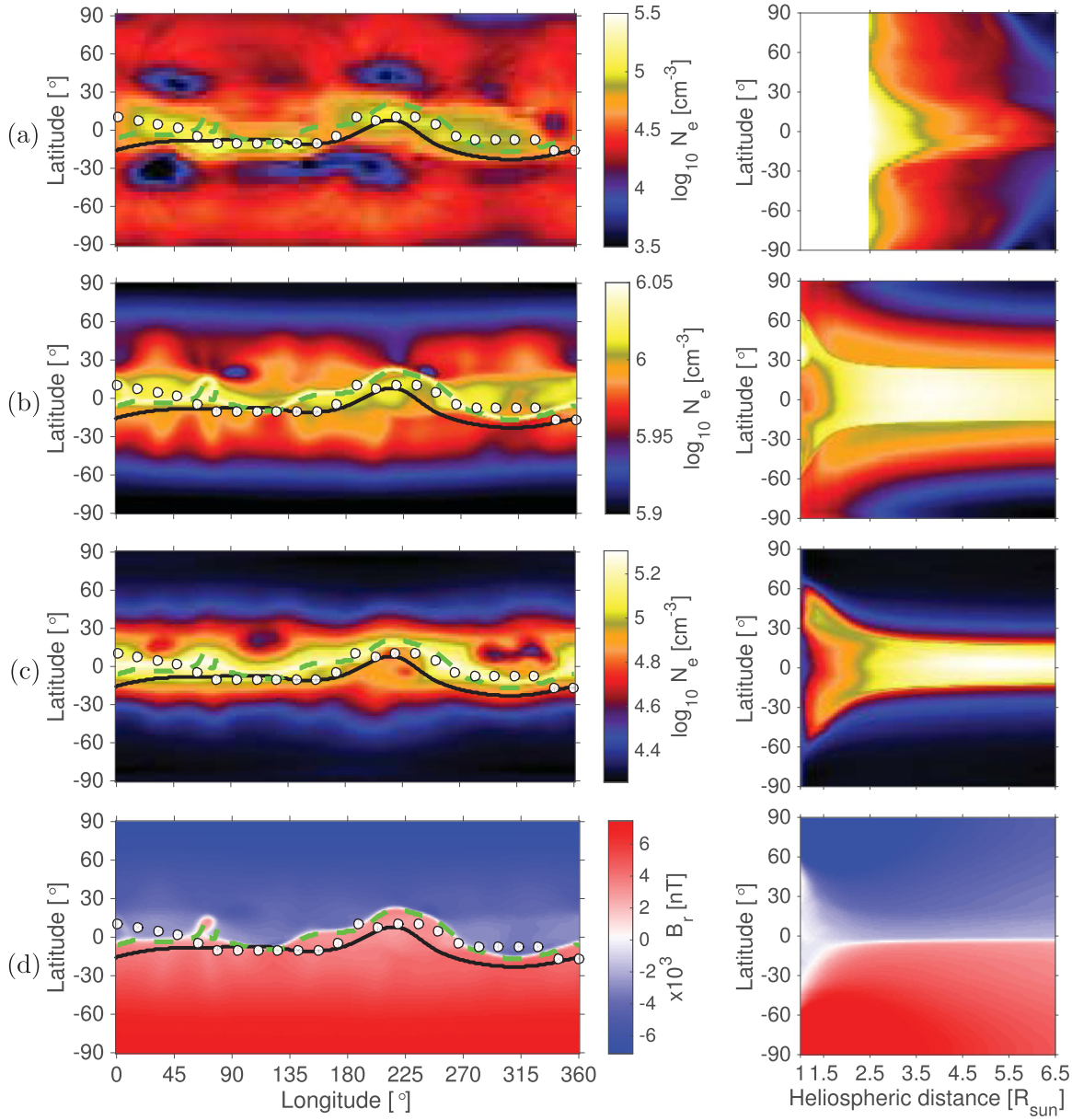

Figure 2. (a) N_e from tomography (2008 November 21 to December 4). MHD solutions for Carrington rotation 2077: (b) polytropic pMHD/N_e, (c) thermodynamic tMHD/N_e, and (d) polytropic pMHD/B_r. The left side shows the longitude–latitude map at 3.5 $R_\odot$. See text for an explanation of the plotted lines. The right panel shows the latitude–radial maps obtained by integrating over the longitudes in tomographic and MHD/N_e solutions, and by a median over the longitudes in the pMHD/B_r solution (radial contrast enhancement has been applied).

the magnetic field, such as the location and evolution of coronal holes, streamer structures, and the HCS; however, such an approximation does not predict the density and temperature very accurately (Riley et al. 2006). In particular, Vásquez et al. (2008) compared a static tomographic reconstruction of the density with two polytropic MHD models (Stanford: Hayes et al. 2001; Michigan: Cohen et al. 2007) during Carrington rotation 2029. They found that these polytropic MHD models could reproduce the density values only below 3.5 $R_\odot$ and at low latitudes, while both models had problems reproducing the correct density in the polar regions. A more recent thermodynamic MHD model uses an improved equation for energy transport in the corona that includes parallel thermal conduction along the magnetic field lines, radiative losses, and parameterized coronal heating. This thermodynamic MHD model produces more accurate estimates of plasma density and temperature in the corona (Lionello et al. 2009; Riley et al. 2011). The electron density estimated by the polytropic MHD model (pMHD/N_e) for Carrington rotations 2077 and 2097 are shown in panels (b) of Figures 2 and 3, respectively. Panels (d) show the radial field calculated by the polytropic MHD model (pMHD/B_r) for the same Carrington rotations. The density predicted by the thermodynamic MHD model (tMHD/N_e) is shown in panels (c) of Figure 2 for Carrington rotation 2077. In the left panel, we show the longitude–latitude Carrington map at 3.5 $R_\odot$; in the right panel, we show the latitude–radial map obtained by averaging over the longitudes. The latitudinal locations of the density maximum in pMHD/N_e are shown as a green dashed line. The latitudes of the density maximum in tMHD/N_e for the thermodynamic MHD model are nearly identical since both models reproduced the general observed configuration of the magnetic field.

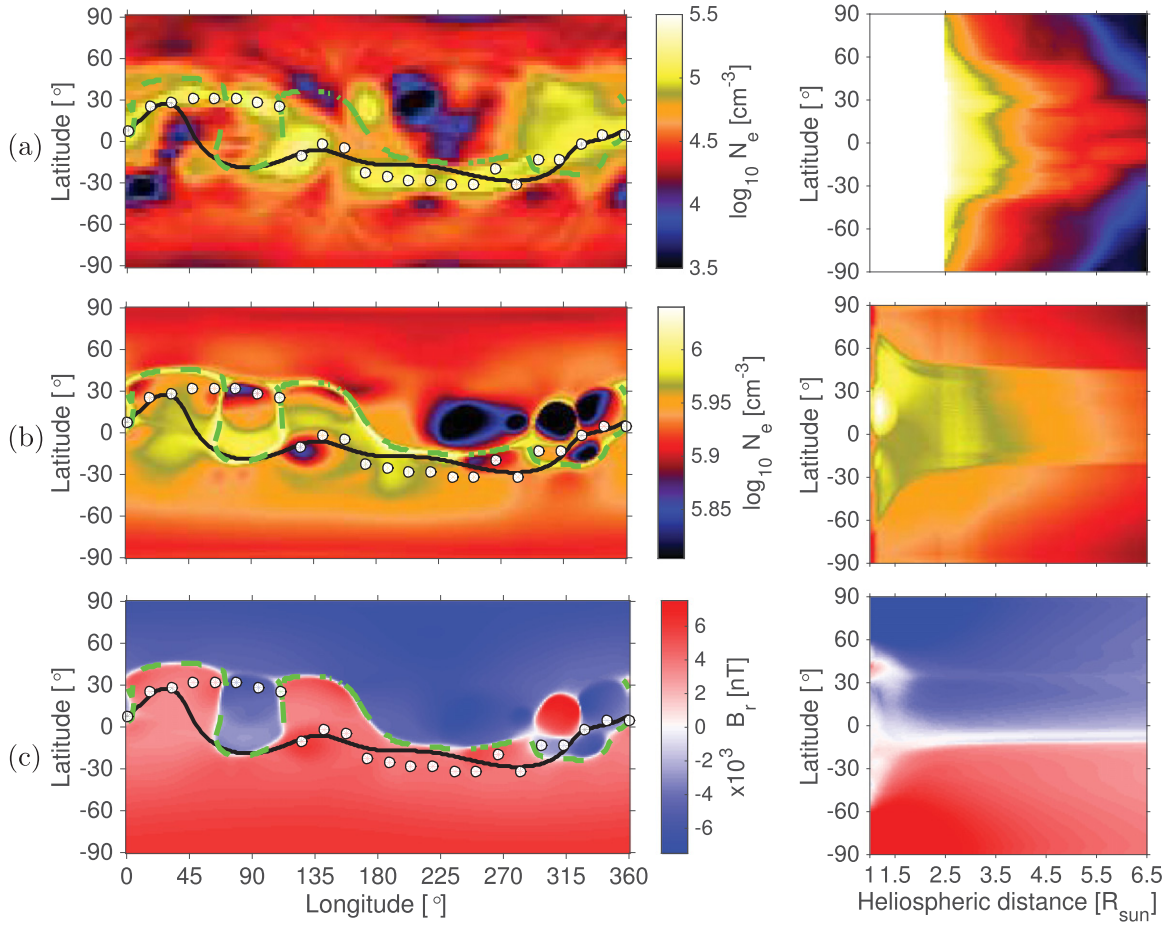

Figure 3. Same as Figure 2. (a) Tomographic solution from 2010 June 6 to 20. Polytropic MHD solution for Carrington rotation 2097 in (b) and (c).

It is important to note that the PFSS and the global MHD models require a series of magnetograms providing the nearest central meridian data on the photosphere and covering a full Carrington rotation (27.2753 days), while tomography requires observations of the coronal emission covering only half a rotation, since it relies on optically thin measurements. Moreover, the photospheric measurements beyond 75° absolute latitude are not reliable owing to the larger viewing angle with the magnetic field. Therefore, errors in polar field strength estimation at the surface can lead to discrepancies in the modeled magnetic field configuration of the corona. This is especially true during the solar minimum, when the polar fields are the strongest.

3. ANALYSIS AND COMPARISON

The overall density structure from the MHD models reproduces the essential features of tomography. Nevertheless, we can see that the results obtained from tomography are more structured, in particular at the poles. The location of the density maximum in pMHD/N_e and tMHD/N_e (green dashed line, Figures 2 and 3) follows nearly exactly the HCS predicted by pMHD/B_r, which is expected since the models MHD/B_r and N_e are not independent. We observe a clear mismatch between the locations of highest densities from tomography (white dots), the PFSS/HCS (black line), and the density maximum from the MHD solution (green dashed line). Previous works showed a limitation of the PFSS model in adequately reproducing some of the observed magnetic structures, in particular when large parts of the solar atmosphere are filled with nonpotential magnetic fields owing to the presence of active regions (Wang et al. 2007; Kramar et al. 2014). Here we show that this is also the case for the HCS predicted by the MHD solutions. The density values found for pMHD/N_e spread over a narrower range (6.3×10^5–1.3×10^6 cm^{-3}) and overestimate the tomography values (3.1×10^3–3.2×10^5 cm^{-3}) by an order of 4 for the maximum values and up to 10^2 for the minimum values. Our comparison illustrates the extent to which the plasma parameters predicted by the polytropic MHD model are less realistic compared to the thermodynamic values tMHD/N_e (1.9×10^4–1.9×10^5 cm^{-3}). Typical histograms of the density distributions over the radial distances in Figure 4 show that tomography provides a larger range of density values at every solar radius.

3.1. Temporal Evolution and Radial Profiles of the Density

To investigate the temporal evolution of the density during the two solar cycle minima, we first average over longitude all solutions obtained from tomography, pMHD/N_e, and the thermodynamic MHD solutions (tMHD/N_e), as was done for Figures 2 and 3, right panels of (a) and (b). We evaluate the "maximum equatorial" electron density, $P_{N_e}^{eq}(r, t)$, by taking the maximum density value over the latitudes at each radial distance. We evaluate the "polar" electron density, $P_{N_e}^{pl}(r, t)$, by averaging the density values obtained above 65° and below −65° latitude at each radial distance. Figure 5 shows the temporal evolution of these densities in the equatorial (red) and

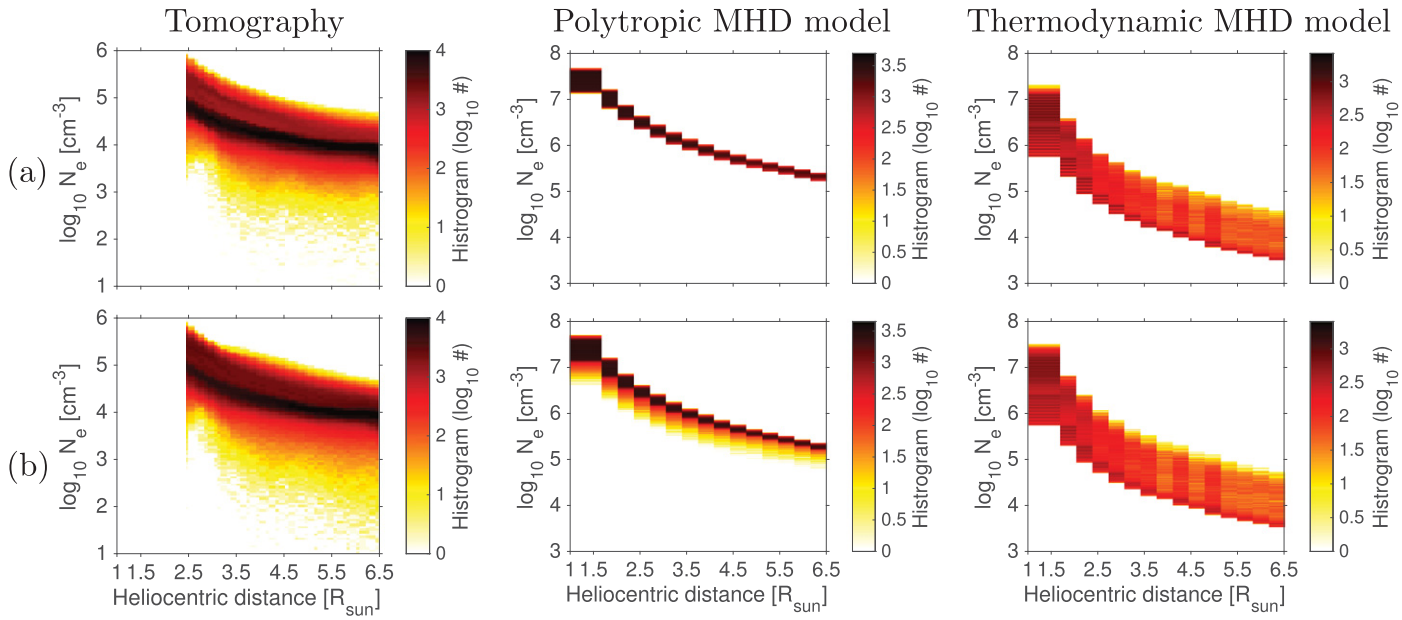

Figure 4. Histograms of the density distribution for the radial distances. (a) Tomographic result for 2008 November 21 to December 4, and MHD solutions for Carrington rotation 2077. (b) Tomography: 2010 June 24 to July 8, and MHD solutions for Carrington rotation 2098.

polar (blue) regions at a radial distance $r = 3.5\ R_\odot$. Since the thermodynamic MHD model is more complex and takes more time to compute, we have fewer data solutions.

We note first that the temporal evolution of the density distribution from tomography shows a good agreement with the solar cycle; for reference we show the daily sunspot number (SN) and the yearly smooth SN in the top panel of Figure 5. In particular, the density values at the equator are found to be lower during the 2008–2010 solar sunspot minimum ($N_e \sim 0.8 \times 10^5$–$1.1 \times 10^5\ \mathrm{cm}^{-3}$) compared to the 1996–1998 minimum ($N_e \sim 1.5 \times 10^5$–$2.0 \times 10^5\ \mathrm{cm}^{-3}$). The minimum in 2008–2009 had 818 days where no sunspot was recorded, with a yearly smooth SN $\geqslant 2.1$, while the minimum in 1996–1997 had only 309 spotless days, with a yearly smooth SN $\geqslant 10.4$. To assess our methodology, we also show the values found by Saito et al. (1977) at $r = 3.5\ R_\odot$ (squares) at the equator ($1.8 \times 10^5\ \mathrm{cm}^{-3}$) and in the polar regions ($0.5 \times 10^5\ \mathrm{cm}^{-3}$). Saito's densities were evaluated during a previous minimum (solar cycle number 20/21, with 272 spotless days and a yearly smooth SN $\geqslant 16.9$); nevertheless, Hayes et al. (2001) and Quémerais & Lamy (2002) observe good agreement during the first minimum for polar and equatorial regions. At the equator, we consider the higher-density values, while these authors estimate average values of density. The second minimum, in 2008–2010, shows a lower SN, which reveals how tomography can reproduce the variation of the density distributions that follow the solar cycle. At the poles, the density from tomography is about 40% that of Saito's for both minima. The density models from Saito et al. (1977), Hayes et al. (2001), and Quémerais & Lamy (2002) are evaluated using the axisymmetric assumption, which is less reliable than a tomographic inversion. During the separation of the K component in the processing and the calibration of the pB images, an overestimation of the F corona and the stray light cannot be excluded, which results in underestimating the K component and thus the estimated density. On the other hand, these models might also suffer from the misestimation of the background, resulting in incorrect higher values. In the future, a new calibration procedure as proposed by Morgan (2015) could be used to refine these results.

As already noted, pMHD/N_e overestimates the density found in the tomographic reconstruction by an order of magnitude. On the other hand, tMHD/N_e provides more accurate values of the density albeit overestimated at the equator (tomo/tMHD $\sim 52\%$) and underestimated at the poles (tMHD/tomo $\geqslant 70\%$). These differences could be linked to the way the equatorial and polar values are computed: recall that the equatorial values correspond to maximum values, while the polar values are averages. It would appear more difficult to obtain a true maximum of a local parcel of plasma with the tomography than it is with the MHD simulation. The lack of resolution at the poles could explain the lower densities in the tMHD model. No significant time evolution can be observed in pMHD/N_e, while the tMHD/N_e values show time variations that follow the variations in tomography estimates during the minima of the two solar cycles. This is more obvious for the equatorial regions and during the second more extended solar minimum. Therefore, we conclude that the main variations found in the tomography results are realistic and can be physically interpreted by changes in sunspot activity.

We next study the differences between the two solar minima and estimate radial profiles for the tomographic, pMHD/N_e and tMHD/N_e results. The "equatorial" radial profiles are obtained by averaging the electron density profiles as follows:

$$\langle P_{N_e}^{\mathrm{eq}}(r,t)\rangle_{1996<t<1997} \quad \text{and} \quad \langle P_{N_e}^{\mathrm{eq}}(r,t)\rangle_{2008<t<2010}.$$

Similarly, we estimate the "polar" radial profiles of the density:

$$\langle P_{N_e}^{\mathrm{pl}}(r,t)\rangle_{1996<t<1997} \quad \text{and} \quad \langle P_{N_e}^{\mathrm{pl}}(r,t)\rangle_{2008<t<2010}.$$

Figure 6 shows those radial profiles of the density for the first minimum ($1996 < t < 1997$) as a dashed line, for the second minimum ($2008 < t < 2010$) as a solid line, at the equator (red) and at the poles (blue). Error bars represent the variance of the density values in the tomographic reconstruction over the given time period. As a reference, we also show the radial

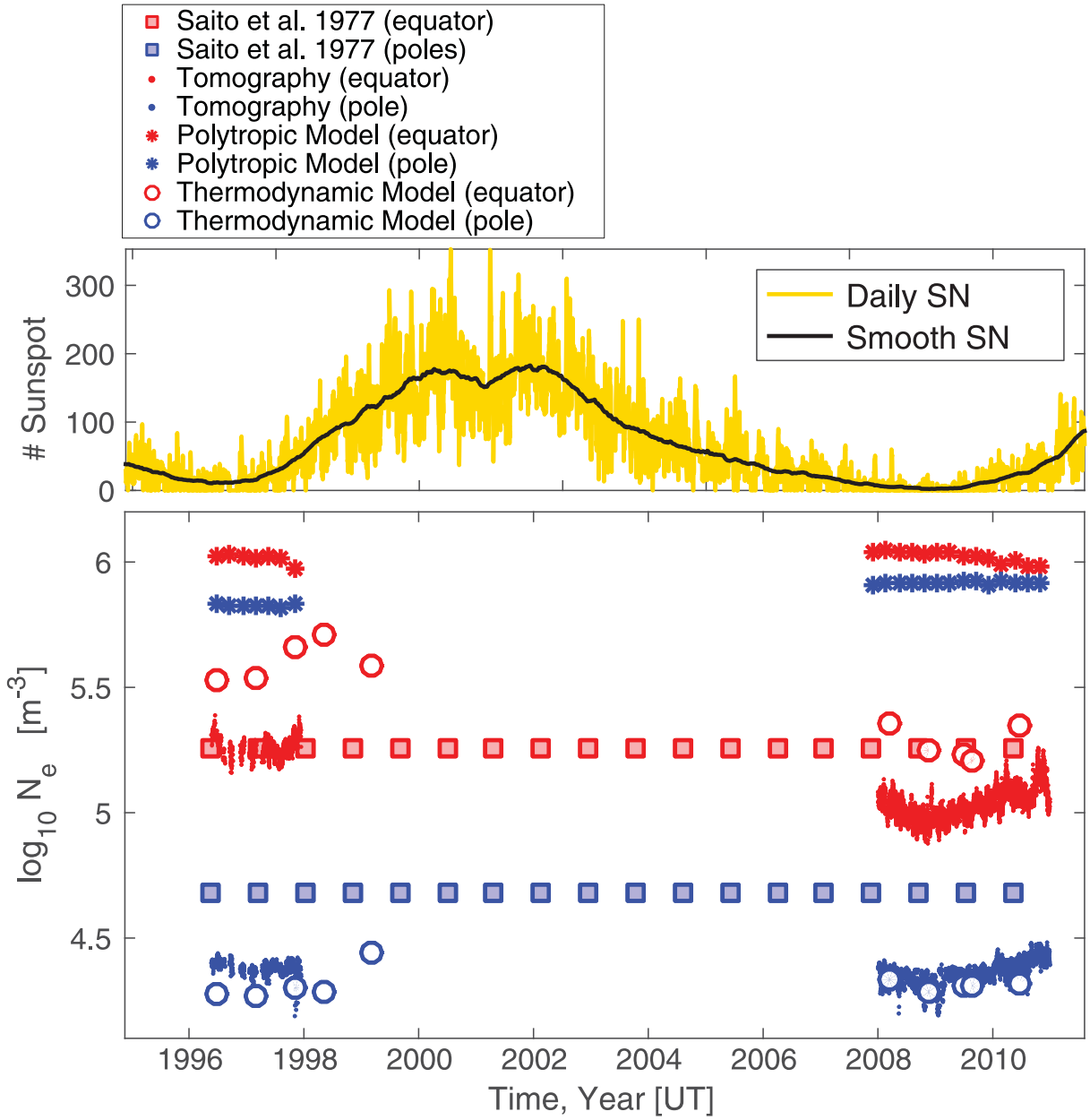

Figure 5. Top: sunspot number (SN) (Source: SILSO World Data Center (1996–2012), 2015). Bottom: electron density evaluated at 3.5 $R_\odot$: maximum values of the density are shown in red, and average values at the poles are shown in blue.

profiles found by Saito et al. (1977). The general radial profile trends are in reasonably good agreement. Tomography results show profiles slightly more complex, and important changes between the two solar minima are observed. First, at the equator the densities differ by 62% along the radial profile, showing that the variations between cycles at 3.5 $R_\odot$ are found at all radial distances. Second, at the poles the profiles cross at 3.5 $R_\odot$, showing opposite variations between cycles, below and above this key radial distance, with larger densities in the outer corona during the second deeper minimum. While the tMHD/N_e profiles at the equator differ by a larger factor of 92% between the two minima, there is no significant change at the poles. The tMHD/N_e profiles are more consistent with tomography up to 3.4 $R_\odot$ and produce lower values at larger radial distances.

3.2. Location of the Highest-density Structures

During the 2008–2010 minimum, comparing the two latitude–radial maps in the declining phase of cycle 23 and the rising phase of cycle 24 (right panels (a) of Figures 2 and 3) helps to show that the denser region, presumably above active regions, spread more in latitude when solar activity increases. It is not obvious that the denser regions always correspond to the helmet streamer.

We investigate how locations in latitude of the density maximum and the HCS agree or differ with time during the 2008–2010 minimum. To do so, we estimate the position in latitude of the density maximum in all the tomographic reconstructions and in the pMHD/N_e models for every Carrington rotation from 2065 to 2106. The latitude of the HCS is extracted both in the PFSS model at the source surface of 2.5 $R_\odot$ and in the pMHD/B_r model (as the neutral line where

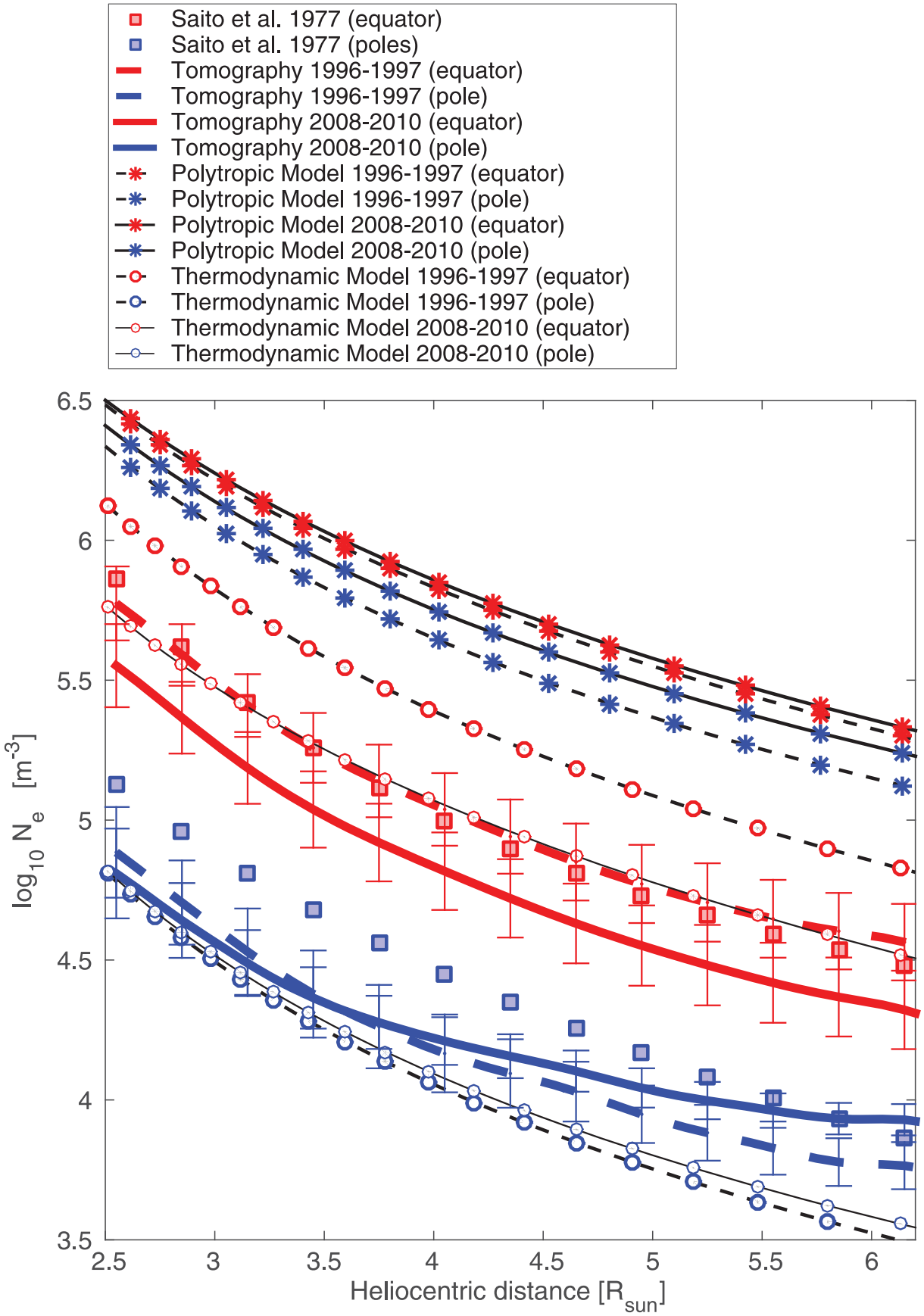

Figure 6. Radial profile of the electron density. Maximum values of the density are shown in red, and average values at the poles are shown in blue.

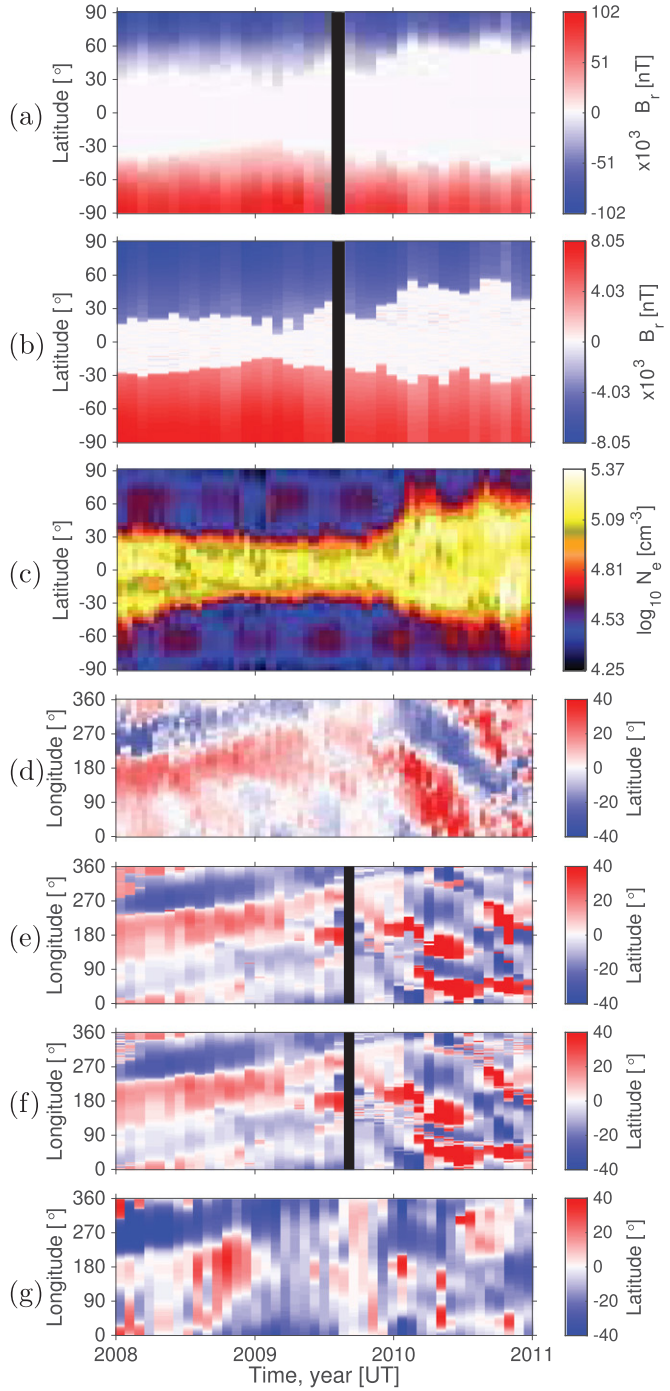

Figure 7. Relations between electron densities and the HCS during the 2008–2010 solar minimum. Latitude–time map of the closest-to-zero radial magnetic field predicted by pMHD/Br at (a) 1.5 and (b) 3.5 $R_\odot$, showing the range of latitudes for the HCS, and (c) latitude–time map of the higher density over longitudes obtained from tomography at 3.5 $R_\odot$. Longitude–time map of the latitudinal locations of the density maximum at 3.5 $R_\odot$ from tomography in (d) and predicted by pMHD/N_e in (e). (f) Latitudinal position of the current sheet predicted by pMHD/B_r at 3.5 $R_\odot$, and (g) the PFSS/HCS at the source surface (at 2.5 $R_\odot$). The values of the latitude have been truncated above 40° in absolute value. The black strips correspond to lacking MHD solutions owing to the missing *SOHO*/MDI synoptic map.

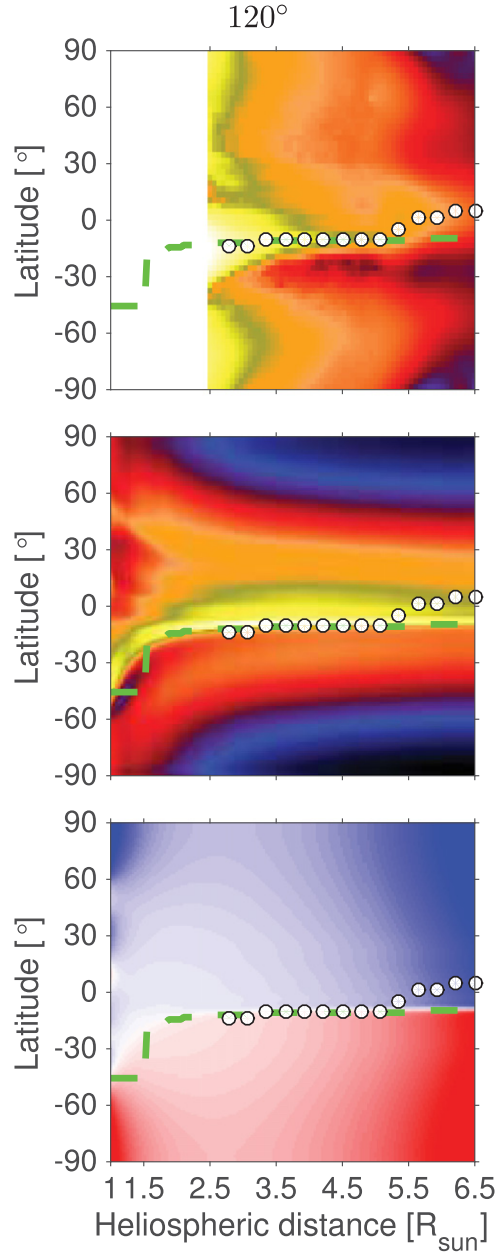

Figure 8. Latitude–radial maps at 120° longitude. Top to bottom: tomographic result (2008 November 21–December 4), pMHD/N_e, and pMHD/B_r (Carrington rotation 2077).

$B_r \simeq 0$) at 1.5 and 3.5 $R_\odot$. Panels (a)–(c) of Figure 7 show the time evolution of the spread in latitude over all longitudes from the HCS predicted by pMHD/Br and the higher-density regions in tomography. Panels (d)–(g) are longitude–time maps that show the latitudinal locations of the density maximum from tomographic reconstructions, pMHD/Ne, and the HCS from pMHD/Br and PFSS. While panels (a) and (b) show that the spread of the HCS predicted by pMHD/B_r is more confined with higher radial distance from 1.5 to 3.5 $R_\odot$, the longitude–time maps of pMHD/B_r were found to be the same at 1.5 and 3.5 $R_\odot$ in panel (f). The latitudinal spread of the tomographic highest-density region in panel (c) follows well the predicted HCS spread in panel (b), notably with a widening of the latitude range at the end of 2009. This change coincides with the rise of the new solar cycle 24 when new sunspots appear at higher latitudes, which results in the streamer belt spanning over higher absolute latitudes. As expected, the results from pMHD/N_e and pMHD/B_r in panels (e) and (f) are nearly the same, which show a good agreement between the

location of the density maximum and the location of the current sheet predicted by the MHD solution. We see a reasonably good agreement between the PFSS/HCS in panel (g) and the current sheet predicted by pMHD/B_r, which is expected since both are based on the observed LOS measurements of the photospheric magnetic field and uniform characteristic values for the plasma density and temperature as lower boundaries. The tomographic highest-density structure generally follows the predicted HCS as observed by Kramar et al. (2014), especially close to the minimum of solar activity, from 2008 to mid-2009. Here this can be observed thanks to longitudinal drifts with time of the highest-density structures. However, this is less clear during the rising phase of solar cycle 24, toward the end of 2009. To investigate this difference, we show latitude–radial planes in the extended minimum and rising phases of cycle 24. Figure 7 shows latitude–radial planes at longitude 120° of the tomographic reconstruction (2008 November 21 to December 14) and of the pMHD/N_e and pMHD/B_r solution during Carrington rotation 2077. In this period of extended minimum, the maximum density in tomography follows the current sheet predicted by pMHD/N_e and pMHD/B_r. On the other hand, Figure 9 shows two examples of planes taken during the rise of solar cycle 24 at longitude 90° and 170° during Carrington rotation 2097, where we observe that the maximum density from tomography does not follow the HCS but more likely aligns with a pseudo-streamer.

Therefore, a pseudo-streamer can be found to be denser than a helmet streamer at the same longitude. We conclude that the highest-density structures do not always correspond to the predicted large-scale HCS or its helmet steamer but can follow the locations of pseudo-streamers. Since both structures contribute to the denser regions near the equator, both play a role in the wider spread in latitude as the activity increases.

3.3. Longitudinal Drifts of the Highest-density Structures

Longitudinal drifts with time of coronal structures at 4 $R_\odot$ have been first reported by Morgan (2011a, 2011b). The author measured the rotation rate of structures within specific latitudinal regions (as opposed to the maximum of density studied here) between −80° and 80° using a back-projection tomographic method. The rotation rates were found to vary considerably between latitudes with values between −3° and 3° d^{-1} relative to the Carrington rotation rate. In Figure 9 we observe a longitudinal drift at 3.5 $R_\odot$ of the highest-density structures that are toward higher longitudes in the extended minimum phase and toward lower longitudes in the rising phase. Knowing how the denser regions are spreading in latitudes as the activity increases, we propose that the highest-density structures show a differential rotation well above the surface depending on how they are magnetically connected to the surface. The tomographic reconstruction method and the MHD models use the approximation of solar Carrington rotation. The Carrington rotation rate of 27.2753 days corresponds to the rotation observed near ±30° latitudes on the surface of the Sun (e.g., Snodgrass & Ulrich 1990; Beck 2000). Thus, depending on the latitude of a structure on the surface, its rotation rate, ω in °d^{-1}, is larger or smaller than the Carrington rotation rate, $\omega_{CR} = 13.20°$ day^{-1},

$$\omega = \omega_{CR} + \alpha, \tag{4}$$

where α is positive for the structures located between the latitudes −30° and +30° (showing a faster rotation), negative for the structures above |±30°| (showing a slower rotation), and zero for structures located near −30° or +30°. During the extended minimum, the helmet streamer clustered near the equator. The structure rotated faster than ω_{CR} and shifted toward the larger Carrington longitudes, resulting in a positive longitudinal drift. From 2008 up to mid-2009, we find a faster rotation rate with $\alpha \simeq 0.25°$ day^{-1}, which means that the structure took only about 26.77 days to make a full rotation. On the other hand, during the rising phase of the solar cycle, the denser regions spread over latitudes above |±30°| and were associated with a negative longitudinal drift. We find a slower rotation rate than ω_{CR} with $\alpha \simeq -0.75°$ day^{-1}, corresponding to about 28.89 days for a full rotation. The reversal in rotation rate coincides with the observed sudden extension in latitudes of the structures associated with the rise of solar activity toward the end of 2009 (panel (c) of Figure 7).

This result shows that the effect of the differential rotation is still visible at 3.5 $R_\odot$, although the structure might not spread above ±30° at this radial distance. It also suggests that the rotation of high-density structures is determined by where they are magnetically connected to the surface of the Sun.

4. CONCLUSION

The 3D electron density distribution in the corona was determined for two solar minima: 1996–1997 (solar cycle number 22/23) and 2008–2010 (solar cycle number 23/24) with both an empirical model from a newly time-dependent tomographic method and theoretical models from both polytropic and thermodynamic MHD solutions. The density distribution is more structured in tomography than in the MHD solutions, in particular in the polar regions. In both MHD models the predicted density distribution is strongly related to the configuration of the calculated magnetic field, and the highest-density structures always follow the HCS. While in tomography the highest-density structures do not always correspond to the predicted current sheet, but can sometimes align with the locations of pseudo-streamers.

In tomographic reconstructions, the highest density at the equator and the average density at the poles follow the temporal evolution observed in the sunspot cycle. The maximum values in thermodynamic MHD solutions, tMHD/N_e, along the HCS show also a solar cycle variation, while there is no temporal evolution in polytropic MHD solutions, pMHD/N_e. This confirms that tMHD/N_e are more realistic values than pMHD/N_e (Lionello et al. 2009). The equatorial values of both tomography and tMHD/N_e are found to be lower during 2008–2010 compared to 1996–1998, in agreement with differences in the solar sunspot minimum. The tMHD/N_e overestimate the tomographic values found at the equator by 52%, while at the poles the values are consistent up to 3.4 $R_\odot$ and then differ. At the poles the density from tomography is about 40% lower compared to Saito et al. (1977) for both minima.

In 2008–2010 the highest-density structures and the HCS predicted by the MHD models show a longitudinal drift, which confirms that the structures do not perfectly follow the Carrington rotation rate, but have a differential rotation also visible well above the surface. Toward the end of 2009 a drastic change in the rotation rate is observed corresponding to the raising of the solar cycle with the emergence of sunspots at higher latitudes and the spreading of the current sheet across

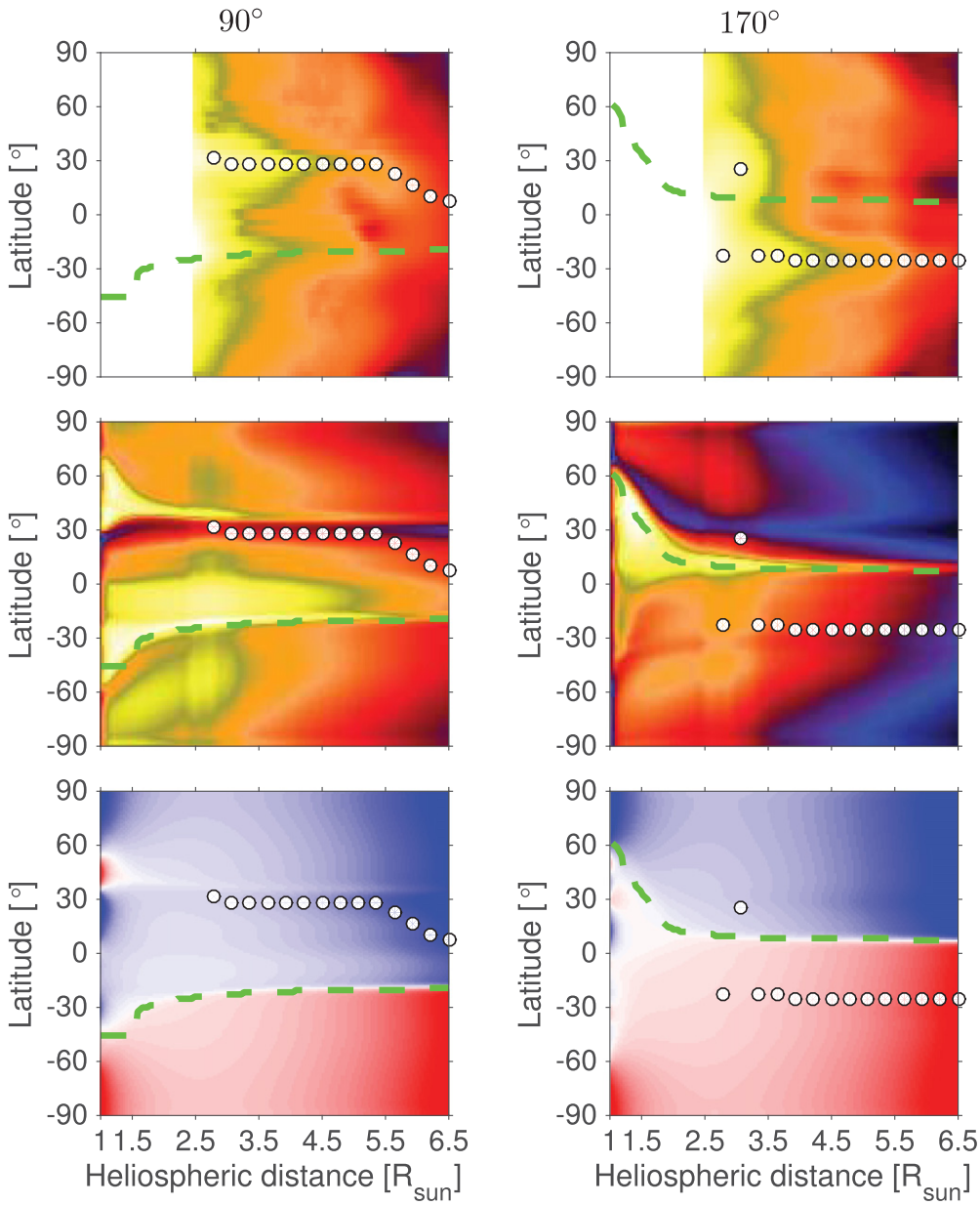

Figure 9. Latitude–radial maps at 90° and 170° longitude. Top to bottom: tomographic result (2010 June 6–20), pMHD/N_e, and pMHD/B_r (Carrington rotation 2079).

the latitudes. The results suggest that the rotation rate of streamers and pseudo-streamers depends on how the structures are magnetically connected to the surface.

The following are possibilities for future investigation: (1) One could identify the specific rotation rates of latitudinal regions or single structures in the corona independently, as done in the study by Morgan (2011b), and contrast the results with an extrapolated radial filed model. (2) One could improve the tomographic method by including the model of the rotation in the reconstruction, as already done by de Patoul et al. (2013b), who included the solar differential rotation modeled only at the surface. (3) Accurate knowledge of the rotation rate of streamers and pseudo-streamers from the surface to higher altitude in the corona could help to better connect the sources of the solar wind to their in situ counterparts (e.g., Foullon et al. 2011; Riley & Luhmann 2012), which can in turn provide valuable insight for future investigations with *Solar Orbiter* (Müller et al. 2013) and *Solar Probe Plus* (Vourlidas et al. 2015). In particular, *Solar Orbiter* will co-rotate with the Sun and provide images of the polar regions from heliographic latitudes above 35°. (4) Ultimately, the time-dependent tomography can be extended to EUV and X-ray ranges to reconstruct also the electron temperature (e.g., Frazin et al. 2009; Vásquez et al. 2009). It can help to constrain the radial density gradients, base densities, and temperatures of global MHD simulations. Such extensions, combined with the MHD coronal modeling efforts, have the potential to increase the reliability for future space weather forecasting.

The authors would like to thank the anonymous reviewer for his/her valuable comments and suggestions to improve the quality of the paper. J.d.P. is the beneficiary of an AXA Research Fund postdoctoral grant. C.F. acknowledges financial

support from the UK Science and Technology Facilities Council (STFC) under her Advanced Fellowship ST/I003649. The *SOHO*/LASCO data used here are produced by a consortium of the Naval Research Laboratory (USA), Max-Planck-Institut for Solar System Research (Germany), Laboratoire d'Astronomie (France), and the University of Birmingham (UK). *SOHO* is a project of international cooperation between ESA and NASA.

REFERENCES

Barbey, N., Auchère, F., Rodet, T., & Vial, J.-C. 2008, SoPh, 248, 409
Barbey, N., Guennou, C., & Auchère, F. 2013, SoPh, 283, 227
Beck, J. G. 2000, SoPh, 191, 47
Bemporad, A., & Mancuso, S. 2011, ApJL, 739, L64
Billings, D. E. 1966, A Guide to the Solar Corona (New York: Academic)
Boursier, Y., Lamy, P., Llebaria, A., Goudail, F., & Robelus, S. 2009, SoPH, 257, 125
Brueckner, G. E., Howard, R. A., Koomen, M. J., et al. 1995, SoPh, 162, 357
Chen, Y., Du, G., Feng, L., et al. 2014, ApJ, 787, 59
Cohen, O., Sokolov, I. V., Roussev, I. I., et al. 2007, ApJL, 654, L163
de Patoul, J., Inhester, B., & Cameron, R. 2013a, A&A, 558, L4
de Patoul, J., Inhester, B., Feng, L., & Wiegelmann, T. 2013b, SoPh, 283, 207
Feng, L., Inhester, B., & Gan, W. 2015a, ApJ, 805, 113
Feng, L., Wang, Y., Shen, F., et al. 2015b, ApJ, 812, 70
Foullon, C., Lavraud, B., Luhmann, J. G., et al. 2011, ApJ, 737, 16
Frazin, R. A. 2000, ApJ, 530, 1026
Frazin, R. A., Lamy, P., Llebaria, A., & Vásquez, A. M. 2010, SoPh, 265, 19
Frazin, R. A., Vásquez, A. M., & Kamalabadi, F. 2009, ApJ, 701, 547
Frazin, R. A., Vásquez, A. M., Kamalabadi, F., & Park, H. 2007, ApJL, 671, L201
Gardès, B., Lamy, P., & Llebaria, A. 2013, SoPh, 283, 667
Hayes, A. P., Vourlidas, A., & Howard, R. A. 2001, ApJ, 548, 1081
Kramar, M., Airapetian, V., Mikić, Z., & Davila, J. 2014, SoPh, 289, 2927
Lamy, P., Barlyaeva, T., Llebaria, A., & Floyd, O. 2014, JGRA, 119, 47
Lionello, R., Linker, J. A., & Mikić, Z. 2009, ApJ, 690, 902
Llebaria, A., Lamy, P., & Danjard, J.-F. 2006, Icar, 182, 281
Morgan, H. 2011a, ApJ, 738, 189
Morgan, H. 2011b, ApJ, 738, 190
Morgan, H. 2015, ApJS, 219, 23
Morgan, H., & Habbal, S. 2010, ApJ, 711, 631
Müller, D., Marsden, R. G., St. Cyr, O. C., & Gilbert, H. R. 2013, SoPh, 285, 25
Peillon, C., Vibert, D., Frazin, R. A., de Patoul, J., & Lamy, P. 2014, Poster Session 5: Origin of Variability and Prediction of Solar Wind, http://www.stce.be/sipworkshop2014/presnpost/extrapost/peillon_poster_SIP7.pdf
Peillon, C., Vibert, D., Frazin, R. A., de Patoul, J., & Lamy, P. 2015, SoPh, submitted
Quémerais, E., & Lamy, P. 2002, A&A, 393, 295
Riley, P., Linker, J. A., & Mikić, Z. 2001, JGR, 106, 15889
Riley, P., Linker, J. A., Mikić, Z., et al. 2006, ApJ, 653, 1510
Riley, P., Lionello, R., Linker, J. A., et al. 2011, SoPh, 274, 361
Riley, P., & Luhmann, J. G. 2012, SoPh, 277, 355
Robbrecht, E., & Berghmans, D. 2004, A&A, 425, 1097
Saito, K., Poland, A. I., & Munro, R. H. 1977, SoPh, 55, 121
SILSO World Data Center (1996-2012). 2015, International Sunspot Number Monthly Bulletin and online catalogue (http://www.sidc.be/silso/)
Snodgrass, H. B., & Ulrich, R. K. 1990, ApJ, 351, 309
van de Hulst, H. C. 1950, BAN, 11, 135
Vásquez, A. M., Frazin, R. A., Hayashi, K., et al. 2008, ApJ, 682, 1328
Vásquez, A. M., Frazin, R. A., & Kamalabadi, F. 2009, SoPh, 256, 73
Vourlidas, A., Howard, R. A., Plunkett, S. P., et al. 2015, SSRv
Vourlidas, A., Subramanian, P., Dere, K. P., & Howard, R. A. 2000, ApJ, 534, 456
Wang, Y.-M., Sheeley, N. R., Jr., & Rich, N. B. 2007, ApJ, 658, 1340
Wiegelmann, T., Thalmann, J. K., & Solanki, S. K. 2014, A&ARv, 22, 78